12-2007

Impact of the Equation of State in Core-Collapse Supernovae

Mark Lewis Baird
University of Tennessee - Knoxville

To the Graduate Council:

I am submitting herewith a thesis written by Mark Lewis Baird entitled "Impact of the Equation of State in Core-Collapse Supernovae." I have examined the final electronic copy of this thesis for form and content and recommend that it be accepted in partial fulfillment of the requirements for the degree of Master of Science, with a major in Physics.

Michael W. Guidry, Major Professor

We have read this thesis and recommend its acceptance:

ARRAY(0x7f7029cb1da0)

Accepted for the Council:
Carolyn R. Hodges

Vice Provost and Dean of the Graduate School

(Original signatures are on file with official student records.)

To the Graduate Council:
I am submitting herewith a thesis written by Mark Lewis Baird entitled "Impact of the Equation of State in Core-Collapse Supernovae". I have examined the final paper copy of this dissertation for form and content and recommend that it be accepted in partial fulfillment of the requirements for the degree of Master of Science, with a major in Physics.

Michael W. Guidry, Major Professor

We have read this dissertation
and recommend its acceptance:

Accepted for the Council:

Carolyn R. Hodges, Vice Provost and
Dean of the Graduate School

Impact of the Equation of State in Core-Collapse Supernovae

A Thesis
Presented for the
Master of Science
Degree
The University of Tennessee, Knoxville

Mark Lewis Baird
December 2007

Dedication

This thesis is dedicated to my parents, for all their support they have given me over the years. To Charlie Leonard, a wonderful teacher who always challenged his students to think outside the box. To Natalie for her friendship. And finally the guy who invented the Big Mac.

Abstract

One of the key ingredients to the core collapse supernova mechanism is the physics of matter at or near nuclear density. Included in simulations as part of the Equation of State (EoS), nuclear repulsion experienced at high densities is responsible for the bounce shock, which initially causes the outer envelope of the supernova to expand, as well as determining the structure of the newly formed proto-neutron star. Recent years have seen renewed interest in this fundamental piece of supernova physics, resulting in several promising candidate EoS parameterizations. We will present the impact of several of their variations in the nuclear EoS using spherically symmetric, General Relativistic multi group Boltzmann neutrino transport simulations of stellar core bounce and shock propagation.

Contents

List of Tables

List of Figures

Chapter 1

Introduction

Stars have always captivated mankind. From the dawn of history mankind has looked up with a sense of wonder and a yearning to understand the universe around us. The Greek astronomer Hipparchus of Nicaea was doing just this in the year 135 BC when he saw a bright light he didn't recognize, seemingly out of place from the night time sky. This light was in the constellation Scorpio and no one could explain what it was, or what its appearance signified. Hipparchus decided to map the entire sky visible from Nicaea. This was one of the first steps taken by the western world to get an understanding of the natural world above and beyond their grasp. These strange new lights in the sky were seen a handful of times there after.

We now know some of these guest stars are much brighter than others because they are supernovae. There are plentiful records of historical supernova sightings. From Chinese and Japanese records we know there were supernovae sighted in 185 AD, 393 AD, 1006 AD and 1054 AD. Unfortunately, it wasn't until much later that mankind began to study these phenomena in greater detail.

In November of 1572, the Danish astronomer Tycho Brahe was walking home and noticed a new star, shining brightly in the con-

stellation Cassiopeia. The next year, he published a book, *De Stella Nova*, which reported his observations of the new star. From the title, we get our modern word "nova". Historically, the term nova was used to mean any star that shined more brightly than usual for a given period of time. Logically a supernova is a star that bursts out with even greater luminosity. We know that the bright star of 1572 was a supernova.

Supernovae can be classified spectroscopically in two distinct groups, Type I or a Type II, according to the lines of chemical elements that appear in their spectra. If a supernova's spectrum contains hydrogen lines, it is classified as Type II, otherwise it is Type I. The Type I classification can be further subdivided according to the presence of other lines and the shape of the light curve. Type Ia supernovae lack the helium absorption line but have multiple silicon absorption lines in their spectra, a clue that the mechanism that creates the supernova may be quite different. Types Ib and Ic do not show lines of hydrogen or silicon absorption. If a star does not have hydrogen in its spectra, but does have non-ionized helium, this is a Type Ib supernova, but if the star does not have hydrogen or helium lines, then it is classified as a Type Ic supernova. Type II supernovae that have a plateau in their light curves are Type II-P. Finally, if the is a linear decrease in magnitude over time, then it is a Type II-L Supernova.

The explosion mechanism between the supernova types is quite different. A type Ia supernova is the result of thermonuclear disruption of a white dwarf that has accreted mass from a companion star. Type II supernovae are massive stars which have run out of fuel at their centers, causing their cores to collapse catastrophically. The mechanism for the progenitors of Types Ib and Ic is likely similar to Type II, but these stars have lost most of their envelopes due to strong stellar winds or interaction with a companion. In this thesis we will focus on core collapse supernovae, Types II and Ib/c.

Initially, a newly-formed star is composed primarily of hydrogen

and helium, approximately 75% and 25% by mass respectively, with a few other trace elements. The hydrogen undergoes fusion in the core for a majority of the star's existence. Once all of the hydrogen in the core has fused to helium, the core contracts because the star is no longer able to offset the gravitational force with its own internal pressure. As the core of the star contracts, densities and temperatures climb, resulting in the fusion of hydrogen in a shell around the He core, which causes the envelope to begin to expand because of the radiation pressure. It will expand several hundred times its original radius or larger depending on the mass of the star. Further contraction leads to helium burning in the core. Once helium burning begins, the star will cease contracting. Where as the star of 10 solar masses was fusing hydrogen for a period on the order of tens of millions of years, fusion of helium into carbon will continue for a few hundred thousand years. It is important to note that the outer envelope of the star is hydrogen, and will remain hydrogen, even through successive cycles of fusion in the core all the way through iron. If the star is massive enough, after helium has been exhausted in the core, the star will repeat the process of contraction until densities and temperatures are reached that will allow carbon to undergo fusion. For massive stars this process will repeat, for neon, oxygen and silicon. Silicon burning will continue in the center of the star until it has produced primarily iron in the core. At this point the center of a star consists of concentric shells of elements much like the layers in an onion. The outside is hydrogen, followed by shells of helium, carbon, oxygen, neon, silicon, and finally iron in the core.

Once the star reaches this point, the process cannot continue because iron has the maximum binding energy per nucleon. Further fusion cycles become improbable because energy is required to fuse iron and heavier elements. The thermal radiation pressure will decrease, and contraction of the core will begin. The contraction of the core is slowed by electron degeneracy pressure. This core con-

traction begins the star's final collapse, from which the core collapse model derives its name. At this point the densities in the core are about $10^{10}\,\mathrm{g/cm^3}$ and the temperature is about 3×10^9 K or 3 GK. At such temperatures and densities, neutrinos produced in the core escape with ease, carrying away energy that could otherwise slow the contraction through radiation pressure. Continued silicon burning in the shell around the iron core causes the iron core to grow. As the iron core approaches Chandrasehkar limit, where degeneracy pressure can no longer balance gravity, the contraction becomes dynamic leading to the collapse of the core. Increasing density leads to copious electron capture and the iron abundance is also being decreased by photo-disassociation caused by the energetic photons; both processes accelerate the collapse.

During collapse the infalling matter will gravitationally accelerate towards the center of the core. Neutrinos will continue to escape and deprive the core of energy until the core densities go beyond $10^{11}\,\mathrm{g/cm^3}$. At this stage steadily increasing opacity limits the neutrinos mean free path and they can no longer escape from the core on the timescale of the core collapse: they are effectively trapped in the collapsing core.

The core continues to collapses until it reaches a critical point where the central densities are greater than that of nuclear matter; at that point a strong repulsive force appears between the nucleons, the core will rebound, and a shock will be formed propagating outward from the core. As the shock moves outward it heats material, disassociating it and leaving high-entropy shocked material behind.

The shock ultimately stalls, usually at a few hundred kilometers from the center. The reason for the stall is primarily loss of energy from the disassociation of heavier elements and increased neutrino emission from the shock heated core, both of which remove available energy and decrease pressure support behind the shock.

The star will either form a neutron star at its core or a black hole, depending on the initial mass of the star. If the star is below perhaps

$20M_{\odot}$, the core is likely to enter a state of hydrostatic equilibrium and form a proto-neutron star (PNS), which will emit neutrinos that will heat the matter behind the shock, and revive it, and leading to an explosion that disrupts the outer layers of the star. This is the delayed explosion mechanism or Wilson mechanism [5].

The neutrinos emitted by the core interact differently with matter depending on its state, with hot matter adding more to the neutrino flux than it removes and thus cooling, and cooler matter being heated by the neutrinos. The gain radius defines the transition from the cooling region near the PNS to the heating region behind the shock. If the matter is reheated sufficiently, the shock will once again begin to propagate outward and produce a supernova.

Over the previous 40 years many models have been attempted to explain the specific physics involved in an exploding star [11]. Physical simulations in one dimension have often failed to produce an explosion able to disrupt the outer layers. One important ingredient in such simulations is the equation of state. This thesis will focus on the effects of different equations of state on modern core collapse simulations. As we will see in succeeding chapters the equation of state play a significant role in the collapse, bounce and post bounce phases of a core collapse.

Chapter 2

Equations of State

As we have seen, gravity and internal pressure compete with each other in the core of the star. To evolve the pressure, as well as other thermodynamic quantities, we require an equation of state (EoS). The EoS is a relationship among thermodynamic variables from the laws of thermodynamics and the micro physical model. For a given temperature (T), density (ρ), and composition ($\mathrm{Y_e}$), the EoS provides pressure, entropy and internal energy information. The electron fraction is defined as the number of electrons per baryon ($\mathrm{Y_e}$). We consider several models for the EoS of nuclear matter. Our first EoS is the Lattimer-Swesty Equation of State (L-S EoS) [1], which uses a compressible liquid drop model and has served as the standard in supernova modeling for more than a decade. We will compare this to the Shen, Toki, Oyamatsu, Sumiyoshi Equation of State (STOS EoS) [2], which uses a Relativistic Mean Field (RMF) model and the Wilson EoS [5].

Densities in the core, prior to bounce, can become quite high, more than $3 \times 10^{14}\,\mathrm{g/cm^3}$. Over the relevant range of densities and temperatures the core is a mixture of protons, neutrons, electrons, positrons, photons and nuclei. Since these are different particles, that follow different statistical processes, their states and occupan-

cies will be different and we must look at each particle type separately to calculate its contribution to the overall equation of state. Because photons are always trapped, they can be treated as a separate ideal Bose gas in thermal equilibrium with the nuclear fluid. Electrons are a fully relativistic, degenerate Fermi gas at densities in the core of the star. The baryons (primarily neutrons and protons) can be either free or bound in nuclei, so some care must be taken in considering their contribution [1]. This is the primary function of the nuclear EoS and the source of the differences between the EoS that we will discuss.

At relatively low densities, approximately $10^{10}\mathrm{g/cm}^3$, and if there is not a large neutron excess, the nuclei are stable and their behavior can be inferred from experimental data. If the density is low, free baryons can also be treated as ideal and the Saha equation may be used to determine abundances [1]. If the temperature and density are higher, then the behavior of the baryons and nuclei is much more complex. As the mass density and neutronization increases during collapse, so does the density of free nucleons, on the whole. However, under some conditions there could be a lowered abundance of nucleons as they form into nuclei. Free nucleons must be treated consistently with nucleons still bound in nuclei. The free nucleons will affect the nuclear surface decreasing the surface tension [1]. Increasing density in the star is often accompanied by an increasing temperature, allowing the constituent particles in the nucleus to become excited [1]. As the temperature increases and approaches the critical temperature where nuclei can no longer exist, care must be taken to find the equilibrium between the nuclear and free nucleon states.

2.1 Lattimer-Swesty Equation of State (L-S EoS)

In the compressible drop model, it is noted that in dense matter the spacing of the free nuclei is of the same order of magnitude as the diameter of the nuclei themselves, which leads to substantial reductions in the nuclear coulomb energy [1]. Translational energy must also be taken into account due to the fact that it may reduce the size of the empty spaces.

L-S EoS uses a Maxwell construction to bridge the gap between the nuclei and nuclear matter regimes. The key is the use of a liquid drop model where the drop maintains thermal, mechanical and chemical equilibrium with its surroundings [1]. The model addresses both the phase equilibrium of nuclear matter, which ultimately determines the densities and the temperature at which nuclei are permitted, and the effects of an external nucleon fluid on the properties of the nuclei [1].

In addition to the original FORTRAN routine, Lattimer now provides a tabular version with $\kappa_0 = 375\,\mathrm{MeV}$ and $E_{sym} = 35\,\mathrm{MeV}$, which I will describe as the Tabular Lattimer-Swesty EoS or L-S Table. This tabular form includes a few notable improvements, particularly correction of an error in the neutron and proton mass difference, which accounts for the differences in the alpha abundance between the L-S EoS and the L-S Table.

2.2 Shen, Toki, Oyamatsu and Sumiyoshi Equation of State (STOS EoS)

The second EoS we will consider is the Shen, Toki, Oyamatsu and Sumiyoshi Equation of State (STOS EoS) [2]. Unlike the L-S EoS, this EoS is based not on the liquid drop model, but on a relativistic mean field [2] with $\kappa_0 = 281\,\mathrm{MeV}$ and $E_{sym} = 36.9\,\mathrm{MeV}$ [3]. Unlike the L-S EoS, the STOS EoS includes only the baryonic contribu-

tions, and depends on meson masses [2]. The electrons are treated at non-interacting relativistic particles, so their contribution must be added separately. For purposes of this work the electron and photon contribution from L-S were used. The use of a consistent electron and photon EoS allows us to focus on the nuclear matter EoS.

2.3 Wilson Equation of State (Wilson EoS)

In the Wilson EoS [5], matter is assumed to be in thermal equilibrium, but chemical equilibrium is not assumed [5]. The Equation of State of Wilson and his collaborators is described in [19, 18, 20]. For supernuclear matter, the empirical prescription of [23] is used with the nuclear saturation density, ρ_0, $= 2.656 \times 10^{14}\, g/cm^3$, the nuclear incompressibility at saturation, κ_0, $= 200\, MeV$ and the supernuclear adiabatic index, γ_0, $= 2.75$. These choices for ρ_0, κ_0, γ_0, as well as the form of the symmetry energy $E_{sym} = 16(1 - 2Y_e)^2(\rho/\rho_0)(1 + 72/(1 + 4\rho/\rho_o))$, were informed by the Relativistic Brueckner-Hartree-Fock calculations of [22]. The Wilson EOS also includes the effects of pion production at high density, using the model of [21]. This model is constrained by comparison between experimental measurements and simulations of pion production in heavy ion collisions [20].

Since all matter particles contribute to the equation of state, they are included, as are photons [5]. Temperature, density and total proton fraction, which are equal to the electron fraction, are the independent variables, which then allows for determination of internal energy, pressure, entropy, as well as abundances. Included in the table are the temperature, density, $\mathrm{Y_e}$, internal energy, entropy, pressure, γ, heavy nuclei abundances, α particle abundances, the average charge number for heavy nuclei, $\bar{\mathrm{Z}}$, and for free baryons, $\bar{\mathrm{z}}$. The average mass of heavy nuclei, $\bar{\mathrm{A}}$, free baryon fractions and baryon

chemical potentials were calculated from the parameters given in the table.

Chapter 3

Comparing Equations of State for Fixed Conditions

For initial testing we used an EoS Tester created by W. R. Hix at Oak Ridge National Laboratory. This allows direct comparison of the EoS for fixed conditions, a stepping-stone to understanding self-consistent collapse simulations with different EoSs. The EoS Tester uses the density, temperature and electron fraction from a prior simulation of core collapse computed with the L-S EoS in AGILE-BOLTZTRAN, which implements fully implicit, multi-group, 4-flavor Boltzmann neutrino transport coupled with implicit spherically-symmetric hydrodynamics with an adaptive mesh [8, 9, 10, 12, 13]. Taking the input data as a function of radius and divided into discrete zones, the EoS tester compares the thermodynamical quantities and abundance data for the various equations of state from the computed profile. Abundance data are returned for neutrons, protons, α particles and a representative heavy nucleus, depending on the current conditions. Mean nuclei mass $\bar{\mathrm{A}}$ and charge $\bar{\mathrm{Z}}$ for the heavy nuclei are also retrieved.

In addition to allowing comparisons of EoS for fixed conditions, without the hydrodynamic feedback, the EoS test allows us test the

subroutines for the various EoS to make sure that they are compatible with AGILE-BOLTZTRAN.

3.1 Implementation

While the EoS tester originally compared LS and STOS EoS, I extended it to use the LS Table and Wilson EoS. Tabular versions of the nuclear matter equation of state are constructed to form a 3-dimensional array (Figure 3.1) monotonically varying in density (ρ_i), temperature (T_j) and electron fraction ($\mathrm{Y_{e_k}}$), with thermodynamical values calculated at each grid point. Since the input values (ρ, T, Y_e) are usually between points in the Equation of State (EoS) table, we use a tri-linear interpolation scheme. Given a set of (ρ,T,Y_e) one must first identify its location in the Table (ρ_i,T_j,$\mathrm{Y_{e_k}}$) such that:

$$\rho_i < \rho < \rho_{i+1} \tag{3.1}$$

$$T_j < T < T_{j+1} \tag{3.2}$$

$$Y_{\mathrm{e_k}} < Y_\mathrm{e} < Y_{\mathrm{e_{k+1}}} \tag{3.3}$$

The triplet i, j, k defines a cube in the table that surrounds the ρ,T,Y_e.

Treatment of the composition data required additional care. While the sum of the mass fractions returned by the EoS equals one, this is not necessarily true for interpolated quantities. In order to avoid this problem and maintain consistency in how the various EoSs handle the abundance values, we computed the heavy fraction from the difference of the combined interpolated values for neutron, proton and α particle fractions from unity.

3.1.1 The STOS EoS Implementation

The first EoS considered was the Shen, Toki, Omyotstu and Sumiyoshi equation of state. The table includes values at intersection points

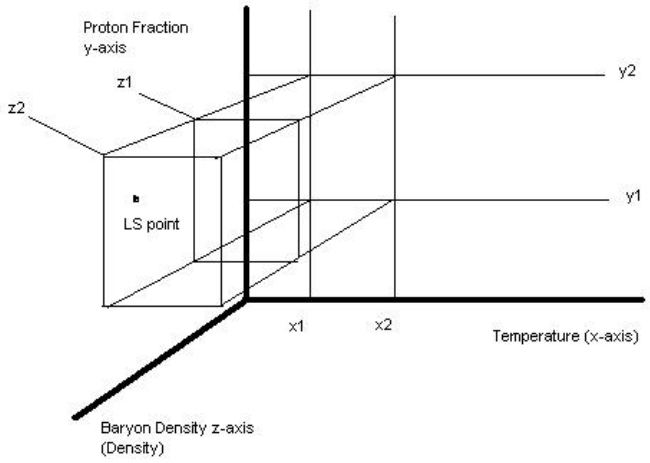

Figure 3.1: A 3-D array for interpolation

where the temperature, density and electron fraction are varied for the desired conditions. The range of the table for the three coordinate values is 0.1 MeV to 100 MeV for kT and 0.001 to 0.5623 for the electron fraction, while the density ranges from $1.26 \times 10^5\,\mathrm{g/cm^3}$ to $2.511 \times 10^{15}\,\mathrm{g/cm3}$. The steps are $\log_{10}$ T = 0.1, $\log_{10}\, Y_\mathrm{e} = 0.025$ and $\log_{10}\, \rho = 0.1$. This gives us 229,000 points where all thermodynamic quantities are defined for collapse conditions. The STOS EoS table required extra attention when reading the data and interpolating because of irregularities in its density grid. Instead of consistent values for the density, the values were found to vary a few percent at high density. Assuming that the table is regular causes incorrect cube corners to be used in the interpolation, this resulted in erroneous coefficients and incorrect interpolated values. To avoid this I used a routine to check all the cube corners prior to interpolation, to verify that the density values were correct regardless of position in the table based on the position of the density with respect to the

j and k coordinates:

$$\rho_{j,k} < \rho < \rho_{j+1,k+1}. \tag{3.4}$$

The internal energy of the STOS EoS was adjusted by 6.2 MeV to reflect differences in the matter configuration defined to have zero internal energy in the STOS table from that defined zero by L-S EoS. Because STOS EoS does not contain lepton or photon information, I used the calculated and summed values from the L-S routine for these contributions to get the full required EoS values. This use of common lepton and photon contribution also helps focus the analysis on the nuclear EoS.

3.1.2 L-S EoS Table Implementation

The Lattimer-Swesty EoS Table was completely regular with respect to density, temperature and electron fraction. The range of the table for the three coordinate values is 0.1 MeV to 31.6 MeV for kT, 0.001 to 0.5000 for Y_e, and baryon density of approximately 1.6×10^7g/cm^3 to 1.6×10^{15}g/cm^3 for the mass density. The steps between successive points in the table are 0.1, 0.01 and 0.1 respectively. This gives us approximately 813,000 points where all thermodynamic quantities are defined.

The one complication in the use of the tabular form was the table's maximum electron fraction of 0.5. As a result an out-of-range error could occur when going out of the bounds of the table. This issue is exacerbated by interpolation because slightly higher values are needed to construct the local interpolation cube corners. To prevent extrapolation, limits were placed in the EoS tester and subsequently in the AGILE BOLTZTRAN code to create a global limit on the electron fraction. The L-S table is a complete EoS, with the electron and photon components included. In addition to the different choice in the compressibility and symmetry energy, the table differs from the routine because the L-S routine produces errant α

particles and heavy-element abundance, which was corrected in the L-S EoS Table.

3.1.3 Wilson EoS Implementation

The Wilson EoS [5] is a complete equation of state, including the electron and photon contributions. The range of the table for the three coordinate values are from 0.005MeV to 150MeV for kT, 0.000 to 0.4990 for the electron fraction, and 1g/cm^3 to 10^{16}g/cm^3 for density. The steps are $\log_{10}$ T = 0.01, Y_e = 0.0125 and $\log_{10}$ ρ = 0.03 with 1,200,000 points in the array. To make the large EoS file more manageable we truncated the table at a density of 10^4 g/cm^3. The Wilson EoS table also has an irregular temperature grid with temperature values that vary systematically with density. To address this problem, I used a routine to verify all the cube corners for temperature rather than assuming the values to be consistent, similar to the treatment for density in the STOS EoS case. To get consistency in the internal energies relative to L-S, we adjusted the Wilson internal energy by 9.1 MeV to better reflect the different matter configurations defined to have zero internal energy.

Testing the Wilson EoS in AGILE-BOLTZTRAN revealed discontinuities near the Fe/Si boundary (10^7 g/cm^3). In order to eliminate this problem and get the EoS to mesh properly across this boundary, we used the Lattimer-Swesty EoS at densities below 10^8 g/cm^3. This approach was also taken by Bruenn, Raley and Mezzacappa in their use of the Wilson EoS [6].

3.2 Results

Comparisons of the internal energies at bounce (Figure 3.1) shows moderate variations between the L-S routine, L-S Table and the Wilson EoS. We see a larger elevation in the STOS EoS from 2×10^{14} g/cm^3 to 3×10^{13} g/cm^3, which varies from the L-S EoS by

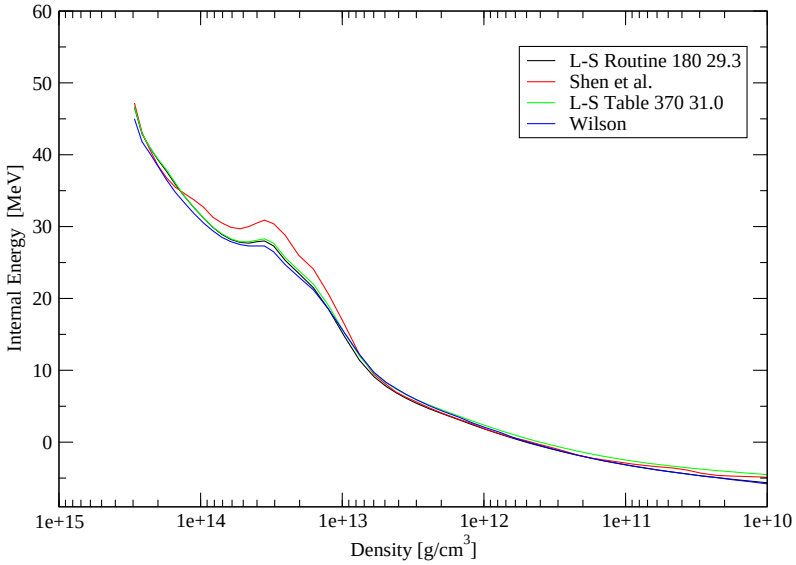

Figure 3.2: Comparison of the internal energy at bounce

as much as 15%. Also we see a deviation appearing at the lower densities, with the highest internal energies in the STOS and L-S Table EoS differing by as much as 17% from L-S EoS. There is a corresponding difference between these EoS and L-S routine α and heavy abundances due to the known errors in the L-S EoS routine (see Figure 3.5).

The comparison of the entropies in Figure 3.2 reveals general consistency between the EoSs in the center of the star through the elevated regions preceding the shock. There is lower entropy for STOS in the very center, however with increasing radius it does quickly reach the level of the other EoS prior to the shocked material (between $1 \times 10^{14}\,\mathrm{g/cm^3}$ to $3 \times 10^{13}\,\mathrm{g/cm^3}$), even climbing above L-S EoSs by as much as 10% at $4 \times 10^{13}\,\mathrm{g/cm^3}$. In densities below the forming shock ($\rho < 10^{12}\,\mathrm{g/cm^3}$), the STOS EoS quickly generates

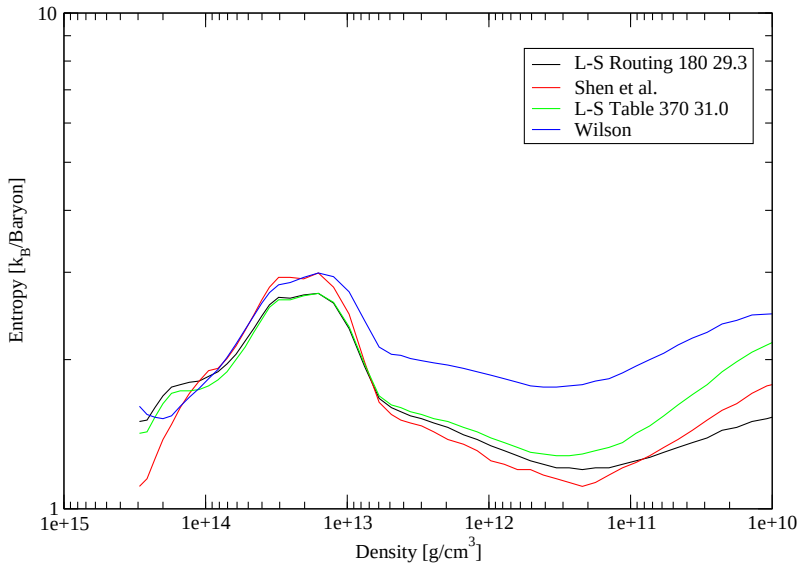

Figure 3.3: Comparison of entropy at bounce

entropies that are similar to the L-S EoS, however the Wilson EoS yields an entropy that is considerably higher, by as much 20% just beyond the shock. These differences increase at lower densities. At 5×10^{11} g/cm^3 the entropies vary by as much as 30% between the Wilson EoS and the L-S and STOS EoSs. These differences in entropy reflect the much larger free neutron fraction calculated in the Wilson EoS.

As the density decreases further, STOS and L-S continue to provide lower entropies then the Wilson EoS. For $\rho < 10^{11}$ g/cm^3 there is a general divergence in the entropies, reflecting the range in α mass fractions calculated by the EoSs. The tabular EoSs have a higher abundances of α particles in the lower densities, with a corresponding decline with the heavy nucleus abundance.

The pressure profile (Figures 3.3 and 3.4) at bounce indicates dif-

ferences between the various EoS. There are differences in the central core, which would affect the neutron star formation and shock evolution. The L-S routine calculates a high pressure in the center of the core with a rapid decrease once we reach a density of approximately 5×10^{13} g/cm^3. This is the region of the proto-neutron star. The material here is composed of free neutrons and protons(Figure 3.5). The α and heavy nucleus fractions are zero. This region is what is giving rise to the high pressures, which once the shock has fully formed 10s of km from center, will help propel the shock out from the central core. The STOS EoS has a higher pressure than the L-S EoS in the region of a few 10^{14} g/cm3, showing that the STOS EoS is stiffer. Wilson has the lowest pressure in this region. Once we move out to regions with greater than 1×10^{14} g/cm^3, we leave the region of nuclear matter for all EoS. In this region the dominant contributions to the pressure are from electrons, with only small deviations reflecting the baryonic compositional differences that also impact entropy.

Examining the abundances in Figure 3.5, we can see interesting differences in what elements are present at various points in core collapse and shock formation. At bounce, there is a high neutron fraction in the central core out to about 10^{14} g/cm^3, the proto-neutron star, and a lower proton fraction corresponding to a ratio of 70 to 30 percent with respect to the free neutron fraction, reflecting the Y_e of the matter. As we move outward in radius, beyond the region of nuclear matter, we see a region dominated by heavy nuclei with heavy nucleus fraction approximately equal to one with the L-S Routine EoS. The L-S Table and STOS EoS show very similar behavior, in this region between 2×10^{14} and 6×10^{13} g/cm^3 with a quick drop off and a subsequent increase in the neutron fraction as we move out from the center of the star. The heavy element fraction for the Wilson EoS, while containing a majority of the mass, is significantly lower than the other EoS, by about 30 percent. The missing mass is in the form of free neutrons and is a significant difference from the

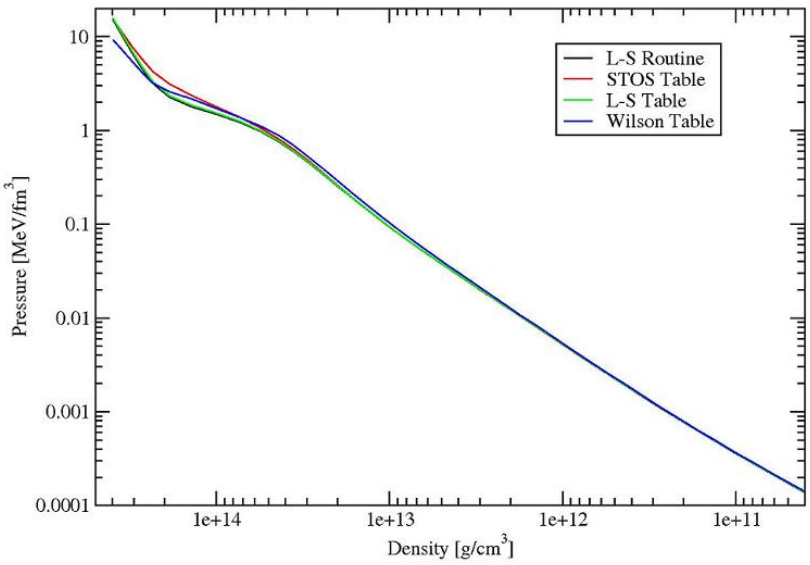

Figure 3.4: Comparison of pressure at bounce

other EoS. For example at 10^{14} g/cm^3 the heavy nucleus fractions are 89% for L-S, 96% for STOS, 72% for Wilson and 89% for the L-S Table. Once we reach a density of 3×10^{13} g/cm^3 all EoSs show $X_{\rm n} \sim 30\%$. The region between 6×10^{13} to 8×10^{12} g/cm^3 marks the shock formation, where heavy elements are being disassociated to form free nucleons and α particles. Beyond this region, for density less than 8×10^{12} g/cm^3, we return to an unshocked region, which is predominately heavy nuclei, with an increasing alpha fraction and decreasing free nucleons as density falls (and $Y_{\rm e}$ approaches .5).

In contrast to the many differences in composition seen near bounce, the composition in the core well after shock formation shows a more homogeneous picture with one important exception. For example, 100 ms post bounce the shock has moved out through the core reaching matter with densities in the range of 5×10^9 g/cm^3.

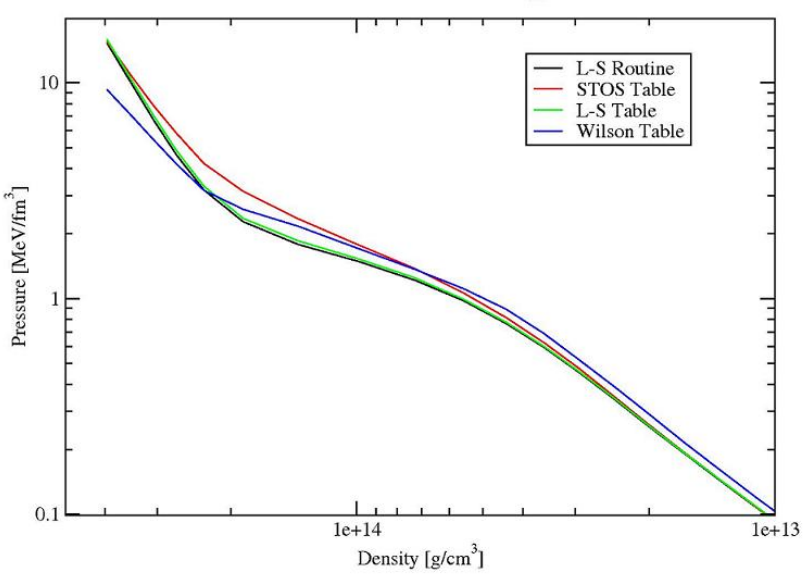

Figure 3.5: Comparison of pressure at bounce, zoomed view

As shown in Figure 3.6 the L-S Routine, L-S table and STOS EoS have only free protons and neutrons in the shock heated gas of the central regions. This is not the case for the Wilson EoS, which shows a large heavy-nucleus fraction between densities of 5×10^{13} g/cm^3 and 2×10^{14} g/cm^3. As a result the Wilson EoS returns a neutron and proton fraction that is significantly below the other EoS.

3.3 Summary

As we have demonstrated in this section, there are significant differences between the respective EoS. STOS shows the highest central pressure as well as a higher internal energy in the forming shock. We see a higher entropy in the Wilson EoS in the unshocked material

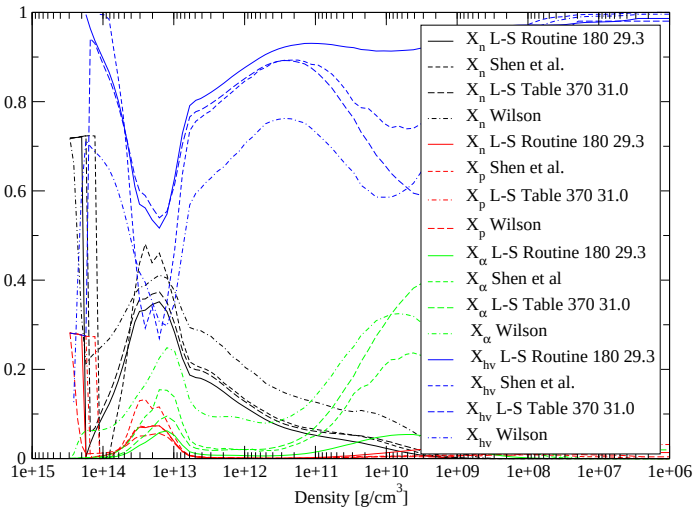

Figure 3.6: Comparison of composition at bounce

with respect to the L-S and STOS EoS, Wilson's EoS also produces a lower pressure in the inner core but yields a higher pressure in the unshocked regions. Also there are significant differences in the particle compositions corresponding to each EoS. Wilson's EoS shows a much larger free neutron dominance through out the core at bounce, with a corresponding drop in heavy nucleus mass fraction. The L-S routine shows a very low α mass fraction for unshocked matter at moderate density, with relatively high heavy nucleus mass fraction. Understanding these differences for fixed conditions will help to understand the effects of the EoS in dynamic simulations.

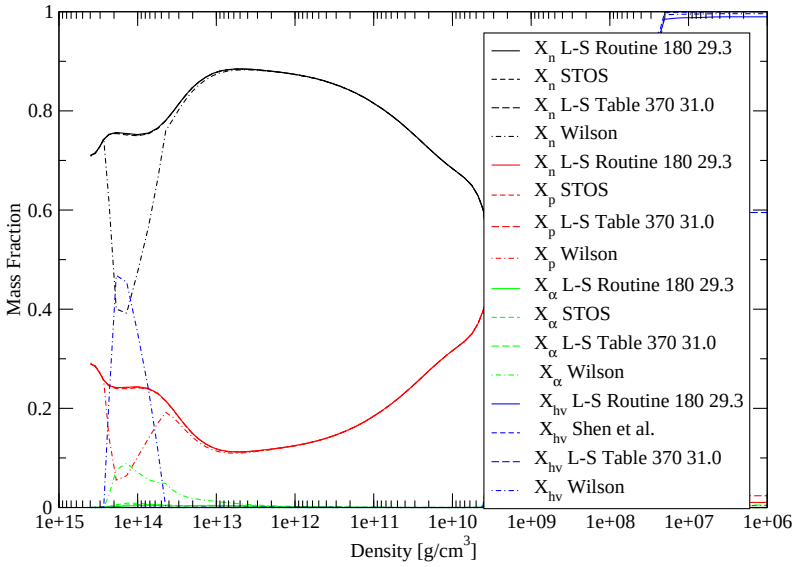

Figure 3.7: Comparison of composition at 100 ms post bounce

Chapter 4

EoS Comparisons in Supernovae Simulations

Using AGILE-BOLTZTRAN, the various EoSs were tested using General Relativistic gravity, with either Bruenn85 [7] electron capture rates or LMSH electron capture table [14, 15]. Evolving the supernova simulation with respect to time, the bounce and long-term evolution for the respective EoSs show the full differences that result from their methodologies. For these simulations we employed 96 radial zones, 6 angles, 12 energy bins in AGILE-BOLTZTRAN and a $15M_{\odot}$ S15B7S2-LMP progenitor [16, 17].

4.1 Comparison at Bounce

Comparing a snapshot near bounce, the point of maximum compression, the differences are apparent. Looking at Table 4.1, the L-S EoS developed a homologous inner core of 0.57 $M_{\odot}$ using the Bruenn85 electron capture rates, with a density of $3.81 \times 10^{14}\,\mathrm{g/cm^3}$ in the center of the star. When LMSH rates were implemented, the core yielded was significantly smaller at 0.48 $M_{\odot}$ and a central core

Table 4.1: Comparison of Equations of State at bounce

At Bounce	Proto-Neutron Star Size (Solar Mass)		Central Core Density (g/cm$\hat{3}$)	
EoS	Bruenn85 EC	LMSH EC Table	Bruenn85 EC	LMSH EC Table
L-S	0.57	0.48	3.81	3.23
STOS	0.60	0.52	3.02	2.67
Wilson	0.62	0.58	3.92	3.42

density of 3.23×10^{14} g/cm3. This difference, demonstrated in detail in Hix et al. [4], result from enhanced electron capture in the core since electron capture on heavy nuclei is not suppressed at higher density as is the case with Bruenn85 electron capture rates.

With the STOS EoS, we see a larger and less dense core with both the Bruenn85 (0.60 $M_{\odot}$) and LMSH electron capture table respectively (0.52 $M_{\odot}$), as compared to the L-S EoS. In both cases, the lower central density results from higher pressure in the STOS core at the relevant densities. The larger cores result from a decrease in deleptonization, which we will discuss in the next section. The Wilson EoS produces the largest proto-neutron star, 0.56 $M_{\odot}$ in the LMSH case and 0.62 $M_{\odot}$ in the Bruenn85 case. Higher densities are reached in the Wilson EoS runs, 3.92×10^{14} g/cm^3 with the Bruenn85 rates and a 3.42×10^{14} g/cm^{3}with the LMSH electron capture rates.

4.1.1 Detailed Comparison of results with LMSH Electron Capture Table

The differences in the initial PNS mass described in the previous section are the result of the deleptonization during collapse. Examining the models using the LMSH electron capture rates, and comparing Y_{e} at bounce, plotted in Figure 4.1, along with entropy, density and velocities, we see that the electron fraction of the L-S EoS case is fairly flat from the central core (Y_{e}= 0.26) to the shock

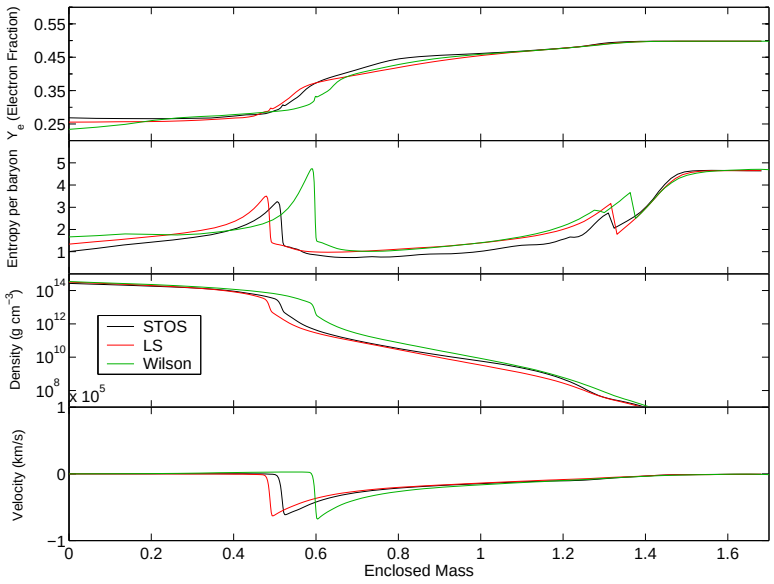

Figure 4.1: Bounce with the LMSH table

(Y_e= 0.28). Once beyond the shock there is a strong jump (approximately 0.1 in Y_e). Above this, in the outer portion of the iron core (from 0.6 $M_\odot$ to 1.3 $M_\odot$), there is a steady increase in Y_e until we reach the Fe/Si boundary, where Y_e reaches a value of 0.5 because of the perfect 28Si gas, which is assumed beyond the iron core. This is unshocked material, where the heavy abundances are still relatively high.

The STOS EoS runs produce higher Y_e, initially at 0.27 in the core, rising to 0.29 at the shock. Once we enter the unshocked material, we see a rise in Y_e consistent with L-S, however, between 0.7 and 1.1 $M_\odot$, there is a Y_e hump produced by STOS where the Y_e is noticeably larger in the STOS case. The STOS case then returns to similar values in the lower density regions where little electron capture occurs, out to the Si/Fe boundary. Comparison

of composition reveals a pattern similar to that discussed in the previous section (see Figure 3.5) with higher heavy nuclei and proton fractions for STOS compared to the L-S EoS out to regions just short of the shock formation, densities ranging from 3.0×10^{14} g/cm^3 to 3.3×10^{13} g/cm^3, with lower neutron and α particle fractions in the same region. When the region of shock formation is reached, there is a reversal of abundances. There is a sharp decrease in the heavy and proton fractions, with respect to L-S EoS, with a corresponding increase in the neutron and α particle fractions. At densities below 5×10^{12} g/cm^3, beyond the shock there is a higher abundance of neutrons and α particles in STOS with a smaller amount of heavies throughout the core of the star. It is this lower X_{hv} which is likely responsible for the Y_e hump around $.9 M_\odot$ in the STOS case.

The Wilson EoS runs return a value of .234 for Y_e in the central core, and unlike L-S or STOS EoS, shows a significant gradient throughout the central core. This is likely the result of the inclusion of pions in the Wilson EoS as the difference occurs in regions where the density is greater than 10^{14} g/cm^3, coincident with the range where the pions impact the EoS [18]. Pions also affect the neutronization of protons by the reactions:

$$\pi^- + p \leftrightarrow n \tag{4.1}$$

$$\pi^+ + n \leftrightarrow p \tag{4.2}$$

These interactions reduce the chemical potential of the protons. As a result, where present, pions effectively increase the temperature and density, as well as decrease the Y_e [18]. In the equibrated region, lower μ_p frees up Y_ν over Y_e, lowering the electron fraction. This leads to a decrease in the Y_e in the inner third of a solar mass, because here the density and temperature are high enough that pions can be created. Beyond this point, the Y_e values are consistent with the other EoS, though displaced slightly near the edge of the homologous core.

The abundance composition is again consistent with the previous section with the Wilson EoS producing a higher fraction of neutron, proton and α particles, and a smaller heavy fraction, as compared to the L-S and STOS EoS, with the exception of STOS in the region of the shock formation. In this region of densities ranging from $5 \times x10^{13}$ g/cm^3 to 5×10^{12} g/cm^3 STOS yields a smaller heavy fraction and a higher neutron fraction. At lower densities Wilson EoS maintains a lower heavy fraction, with higher neutron and α particle fractions.

Examining the entropy, L-S EoS with the LMSH electron capture rates yields a central entropy of 1.34 $k_{\rm B}$/baryon and increases steadily over the inner 0.4 $M_\odot$ out to the shock, where it spikes to 3.50 $k_{\rm B}$/baryon in the forming shock then it falls back to a value of 1.42 $k_{\rm B}$/baryon once we enter the unshocked region. The unshocked region increases gradually out to 1.2 $M_\odot$ where the entropy is 2.08 $k_{\rm B}$/baryon. Beyond this, the entropy again spikes at the Si/Fe boundary at 3.17 $k_{\rm B}$/baryon, falls and again rises to 4.64 in the silicon layers.

Comparing the STOS EoS runs with the L-S EoS models, STOS (Figure 4.1) shows generally lower entropy. Central entropy is 1.00 $k_{\rm B}$/baryon and increases steadily to 0.4 $M_\odot$ before it spiking in the region of the shock to 3.25 $k_{\rm B}$/baryon then the entropy falls back to a value of 0.73 $k_{\rm B}$/baryon in unshocked material. Moving outward, it again increases gradually out to 1.2 $M_\odot$ where the entropy is 1.58 $k_{\rm B}$/baryon. As we near the Si/Fe boundary the entropy increases to 2.74 $k_{\rm B}$/baryon, and then rises to 4.64 in the silicon layers.

The Wilson EoS runs with the LMSH electron capture rates show a flatter entropy profile in the core than L-S or STOS cases with a central values of 1.67 $k_{\rm B}$/baryon and steadily increases until it reaches shocked material (0.5 $M_\odot$, where it spikes to 4.73 $k_{\rm B}$/baryon at 0.6 $M_\odot$. Then the entropy calculated by Wilson EoS falls back to a minimum of 1.01 $k_{\rm B}$/baryon, before gradually increasing out to 1.2 $M_\odot$ where the entropy is 2.24 $k_{\rm B}$/baryon. Beyond this the entropy

again spikes at the Si/Fe boundary at 3.66 k_{B}/baryon, eventually rising to 4.71 in the silicon layers.

Looking at the ρ and velocity comparison, we see that there are differences in the density and velocity resulting from the differences in the deleptonization and energy loss in the core. As to be expected, L-S and STOS EoS exhibit a density cliff marking the edge of the PNS at lower enclosed masses then Wilson EoS, marking the location of the respective shock formation regions. In the unshocked regions there is a higher density for Wilson EoS accompanied by a higher velocity (40% higher than L-S EoS at 0.8 $M_{\odot}$). Nearer to the shock, the velocities are similar, except for an offset resulting from the location of the initial PNS.

4.1.2 Detailed Comparison of results with Bruenn85 Electron Capture Rates

Comparison of models at the point of maximum compression, but this time with models using the Bruenn85 electron capture rates is shown in Figure 4.2. L-S has a Y_{e} of 0.287 at the central core, then decreases out to the shock. Much like the LMSH case, once past the shocked material Y_{e} quickly increases to 0.343 at .64 $M_{\odot}$. Beyond the shocked material it begins a slow increase to the Si/Fe boundary where is normalizes at 0.5 Y_{e}.

As in the previous section, STOS EoS produces a higher Y_{e}, 0.301, decreasing out to the shocked region as does L-S with Bruenn85 electron capture rates. There is a jump in the Y_{e} in the unshocked material just preceding the shock. As before there is a similar Y_{e} hump produced by STOS where the Y_{e} increase is greater than L-S, but then normalizes out to the Si/Fe boundary. In this case, since the Bruenn85 prescription tends to inhibit electron capture on heavy nuclei above 1×10^{10} g/cm^3, the bump is likely the result of lower proton and heavy nucleus abundances as demonstrated in Figure 3.5.

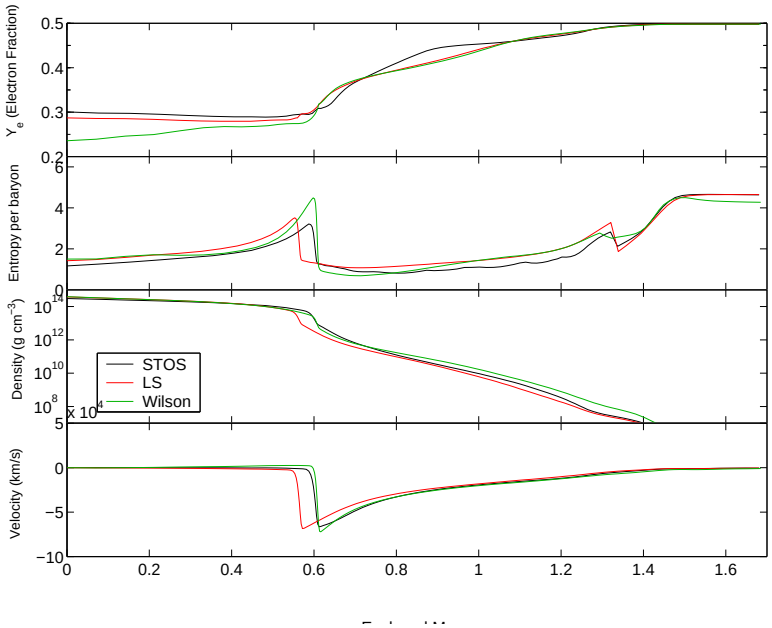

Figure 4.2: Bounce with the Bruenn85 rates

The Wilson case computes a value of .234 for Y_e in the central core, and unlike L-S or STOS EoS, gradually increases out from the central core as was the case in the LMSH electron capture rates because of the inclusion of pions. Beyond this point, the Y_e values are consistent with the other EoS. In the unshocked region Wilson is similar to L-S EoS.

The entropy calculated in models using the L-S EoS with the Bruenn85 electron capture rates yields 1.42 k_B/baryon and increases to 0.57 $M_\odot$, where it spikes at 3.73 k_B/baryon. Beyond the shock, the entropy falls back to a value of 1.08 k_B/baryon, because the material is still unshocked and composed of heavy nuclei and α particles. In the unshocked material, the entropy again increases gradually out to 1.2 $M_\odot$ where the entropy is 2.04 k_B/baryon. Beyond this the entropy again rises at the Si/Fe boundary to 3.27

k_B/baryon, falls and again rises to 4.64 in the silicon layers.

In comparison the entropy calculated using STOS EoS with Bruenn85 electron capture rates is 1.17 k_B/baryon at the center of the core and increases to 0.6 $M_\odot$, where we reach the shock region, where it rises sharply to 3.22 k_B/baryon before falling back to a value of 0.88 k_B/baryon ahead of the entropy again increases gradually out to an enclosed mass of 1.2 $M_\odot$ where the entropy reaches a value of 1.60 k_B/baryon. Beyond this the entropy again spikes at the Si/Fe boundary at 2.83 k_B/baryon, falls and again rises to 4.66 k_B/baryon in the silicon layers.

The Wilson EoS with Bruenn 85 electron capture rates reveal an entropy of 1.66 k_B/baryon in the center. The entropy increases out to 0.62 $M_\odot$ where it reaches shocked material, which it spikes to 4.72 k_B/baryon at 0.5 $M_\odot$, again due to heavy nuclei being disassociated into α particles and nucleons. Then the entropy in these models falls back to a value of 1.02 k_B/baryon when it reaches the unshocked material. The entropy increases gradually out to 1.2 $M_\odot$ where the entropy is 2.184 k_B/baryon. Beyond this the entropy again spikes at the Si/Fe boundary at 3.45 k_B/baryon, falls and again rises to 4.72 in the silicon layers.

Comparing the Y_e and entropy with the ρ and velocity plots, as we have seen before, there are differences in the density and velocity resulting from the displacement of the launch point of the shock. We see the shock drop off in density at lower mass for L-S which has a smaller PNS forming as compared to the STOS and Wilson EoSs. With the Bruenn85 rates the STOS is comparable to the Wilson EoS. This is somewhat different than the LMSH case where the STOS case was closer to the L-S case.

4.2 Comparison at 100 ms Post Bounce

By 100 ms post bounce, hydrodynamic instabilities can begin to play a role in supernova evolution. Most famously, Wilson [18] demonstrates spherically symmetric models which produce explosions as a result of a doubly diffusive "neutron fingers" instability. While one can not fully explore these instabilities in 1D models, we can see how changes in the EoS alter the gradients that drive the hydrodynamical motions, principly the Y_e and entropy gradients.

4.2.1 Detailed Comparison of results with LMSH Electron Capture Table

In Figure 4.3, it can be seen that the models with the L-S EoS and the LMSH electron capture table calculate a Y_e of 0.253 and an entropy of 1.36 k_B/baryon in the center. Y_e decreases with increasing radius to 0.22 at an enclosed mass of 0.37 $M_\odot$ while the entropy increases to 2.89 k_B/baryon Here, in the vicinity of the shock's original launching point, the Y_e experiences a local maximum at 0.24 at 0.57 $M_\odot$. Meanwhile the entropy rate of increase accelerates, before leveling off near 5.0 k_B/baryon in post shock matter. Y_e decreases until 1.1 $M_\odot$ reaching a minimum of 0.11. The entropy again increases steadily in this region before spiking just behind the the shock to 10.47 k_B/baryon.

Simulations using the STOS EoS with the LMSH electron capture table yield a Y_e of 0.27 and an entropy of 1.02 k_B/baryon in the center. Increasing radius shows a decrease in Y_e to 0.21 and an increase in entropy of 2.59 k_B/baryon at an enclosed mass of 0.38 $M_\odot$. Then the STOS EoS case experiences a similar Y_e bump as in the LS-EoS case with a local maximum at 0.49 $M_\odot$ where the Y_e is 0.24 and the entropy of 4.29 k_B/baryon. The entropy continues to climb and reaches a relative plateau at 0.57 $M_\odot$ with an entropy of 4.83 k_B/baryon where the Y_e begins to decrease. The Y_e decrease

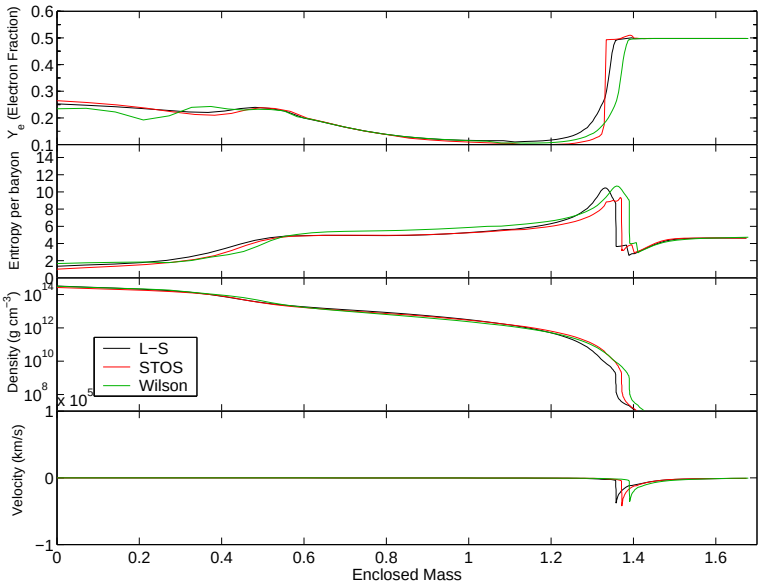

Figure 4.3: 100 ms post bounce with LMSH table

reaches a minimum of 0.10 at 1.2 $M_\odot$ with a corresponding entropy of 5.62 k_B/. The entropy begins to increase in this region as well much more rapidly in the STOS case than in the L-S case. The entropy jumps in the region of the shock to 9.35 k_B/baryon. At the Fe/Si boundary there is an instant transition in Y_e that is not present in the other EoS. Taken together one sees only subtle changes in the location and strength of Y_e and entropy gradient between L-S and STOS models.

In contrast, the models using Wilson's EoS show much larger changes, especially in the inner core. With the Wilson EoS and the LMSH electron capture table, we get a Y_e of 0.234 and an entropy of 1.67 k_B/baryon in the center. There is a wiggle present in the Y_e. Looking at the inner few zones of the core there is a strong Y_e gradient in the range of 0.15 $M_\odot$ to .37 $M_\odot$. At the density and tem-

perature ranges of these zones, this is likely a result of the inclusions of pions interacting with the nuclear matter. Beyond that we see a double hump in the Y_e from 0.37 $M_\odot$ to 0.6 $M_\odot$. In this range there is a large heavy nuclei fraction present, which is quite different from the L-S and STOS EoSs. The entropy levels off at 5.45 k_B/baryon while the Y_e begins to decrease. The Y_e decrease continues until 1.2 $M_\odot$ reaching a minimum of 0.10. The entropy begins to increase in this region as well. The entropy jump at the region of the shock to 10.68 k_B/baryon though the rise is more gentle than in the L-S or STOS cases. Clearly there are significant differences in the entropy and lepton gradients down deep in the models, which merits future exploration.

Giving consideration to the ρ and velocity plots, we quickly recognize the largest difference is the shock location, which varies by 0.04 M_e. Behind the shock, density and velocity are very consistent except for the 2× variations in the density that coincides with the second Y_e hump.

4.2.2 Detailed Comparison of results with Bruenn85 Electron Capture Rates

In Figure 4.4, models using the L-S EoS with the Bruenn85 electron capture rates show a Y_e of 0.283 and an entropy of 1.42 k_B/baryon in the inner core. The Y_e then decreases to 0.230 while the entropy increases to 3.23 k_B/baryon at 0.45 $M_\odot$. Then the Y_e has a local maximum at .53 $M_\odot$ with a Y_e of 0.240 and the entropys rate of increase accelerates. The entropy levels off to 5.74 k_B/baryon when the Y_e begins to decrease. The Y_e decreases to a minimum 1.2 $M_\odot$. In the region through which the shock has passed the entropy begins to increase spiking at the region of the shock at 10.51 k_B/baryon.

Models with the STOS EoS and the Bruenn85 electron capture rates exhibit similar behavior. Figure 4.4 shows a Y_e of 0.294 and an entropy of 1.18 k_B/baryon in the inner core, the Y_e then decreases

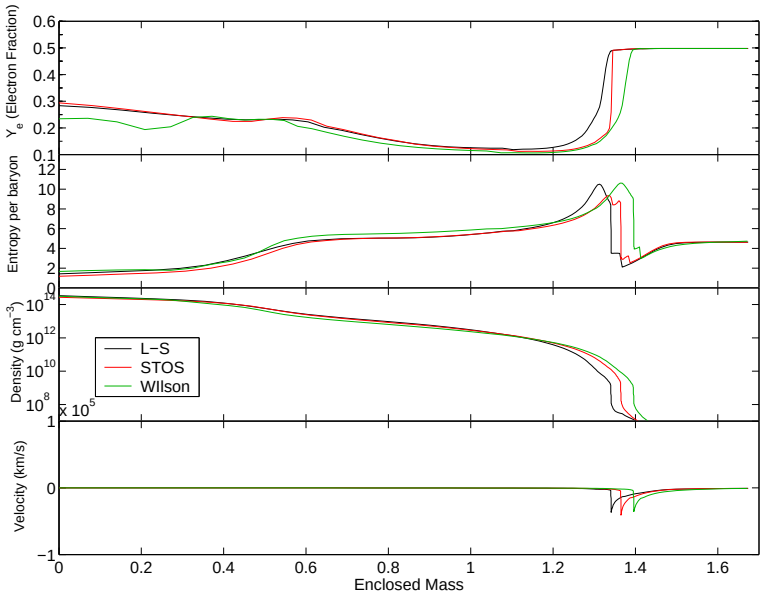

Figure 4.4: 100 ms post bounce with Bruenn85 rates

to 0.224 while the entropy increases to 2.42 at 0.42 $M_{\odot}$ where the $Y_{\rm e}$ experiences a jump at .54 $M_{\odot}$ with a $Y_{\rm e}$ of 0.244 and an entropy value of 4.00 $k_{\rm B}$/baryon. The entropy steadily increases to 5.72 $k_{\rm B}$/baryon while the $Y_{\rm e}$ begins to decrease. The $Y_{\rm e}$ decrease continues until 1.2 $M_{\odot}$. The entropy experiences an in this region. The entropy spikes at the region of the shock at 9.37 $k_{\rm B}$/baryon. As in the case of the LMSH case, STOS also has a quick transition shock, where as L-S EoS and Wilson do not.

Again, as in the LMSH case the Wilson EoS with the Bruenn85 electron capture rates is quite different. It begins with a $Y_{\rm e}$ of 0.234 and an entropy of 1.67 $k_{\rm B}$/baryon in the star's center. Then the Wilson yields a local minimum at .20 $M_{\odot}$ with a $Y_{\rm e}$ of 0.194 with entropy of 1.84 $k_{\rm B}$/baryon. Then $Y_{\rm e}$ increases to 0.37 $M_{\odot}$ with a $Y_{\rm e}$ of 0.244 and an entropy of 2.40 $k_{\rm B}$/baryon. After a brief de-

crease, Wilson EoS yields another hump at 0.46 $M_\odot$ where the Y_e is 0.23 and the entropy is 3.62k_B/baryon. The entropy levels off at 5.35 k_B/baryon when the Y_e begins to decrease. The Y_e continues to decrease out to 1.13 $M_\odot$. The entropy begins to rise in this region as we approach the shock. The entropy spikes in the shock to 10.61 k_B/baryon. Here again we see quite different lepton gradients between the Wilson case and the other EoSs. Interestingly, composition between the LMSH and Bruenn85 cases, both with the Wilson EoS, shows different behavior, highlighting the interaction between the EoS and the other microscopic physics.

4.3 Shock Trajectories

4.3.1 LMSH Electron Capture Tables

The shock trajectories shown in Figure 4.5 (Wilson is blue, L-S is red and STOS is green) provide an important method of contrasting the various EoSs. Beginning at shock launch, out to shock stall, the differences are quite apparent. The small scale wiggles as seen in the figures are not physical, but result from how the location of the shock is determined by AGILE-BOLTZTRAN.

Looking first at the L-S EoS, using the LMSH electron capture rates, we see the shock is launched, and reaches approximately 189 km from the central core before stalling. L-S EoS, where $K = 180\,\mathrm{MeV}$, is considered a soft EoS, and as a consequence releases a larger amount of energy than a stiffer EoS, so the shock will travel further out than a stiffer EoS before stalling, due to energy loses from neutron emission and the disassociation of heavy nuclei.

The STOS EoS is stiffer than the L-S EoS, where $K = 280\,\mathrm{MeV}$, and as a result less energy is stored in compression of the PNS, thus the shock does not travel as far out from the central core, before stalling due to the lose of energy. It reaches only a distance of approximately 165 km before stalling. This maximum also occurs

much sooner (70 ms after bounce) than in the LS mode (100 ms after bounce)

Even though the Wilson EoS is slightly stiffer ($K = 200$) than the L-S EoS, it seems to release more energy than the L-S EoS. This is likely a consequence of the high density pion contribution. It travels out to a distance of approximately 209 km before stall, approximately 20 km further than L-S, and approximately 44 km further than the STOS EoS. Even 200 ms after bounce, the models with those EoSs show a range of 40 km (20%) in the shock location, a clear indication that the EoS is important to the physics of core collapse and bounce, and even times well after bounce.

4.3.2 Bruenn85 Electron Capture Rates

In models using the L-S EoS, using the Bruenn85 electron capture rates as in Figure 4.6, we see the shock is launched, and reaches approximately 187 km from the central core before stalling (again Wilson is blue, L-S is red and STOS is green). This is about 2 km smaller than the LMSH electron capture rates. Also the L-S shock trajectory stalls faster using the LMSH rates than using the Bruenn85 rates, because while the core is smaller and the shock is weaker using the LMSH rates, the electron capture in the outer layers, beyond the shock location has an overall lower electron capture rate and as a consequence have a higher Y_e. This will cause the in fall to be slower, thus providing a lower pressure to oppose the LMSH shock [15].

The STOS EoS reaches only a distance of approximately 173 km before stalling. This is about 6 km larger than STOS EoS with the LMSH electron capture rates. The STOS cases are slightly more affected by the change in electron capture prescription. The shock radius is also 14 km smaller than the L-S LMSH shock radius.

The Wilson EoS again releases more energy than the L-S EoS. the shock radius travels out to a distance of approximately 207 km be-

fore stall, approximately 20 km further than L-S, and approximately 34 km further than the STOS EoS. This is about 2 km smaller than the Wilson EoS LMSH electron capture rates.

Clearly one can see a significant differences in the behavior of the shock well into the neutrino-reheating epoch as a result of the changes in the EoS. From the effects caused by changing the treatment of the nuclear electron capture, one can also see how the impact of the neutrino interactions is affected by the composition provided by the EoS.

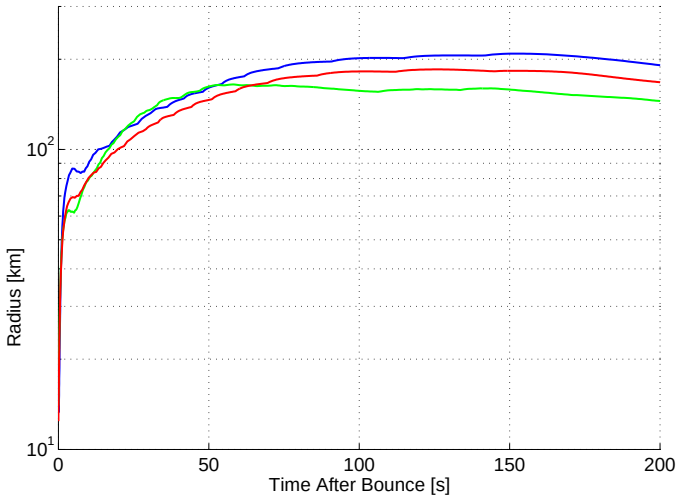

Figure 4.5: Shock trajectory with LMSH table

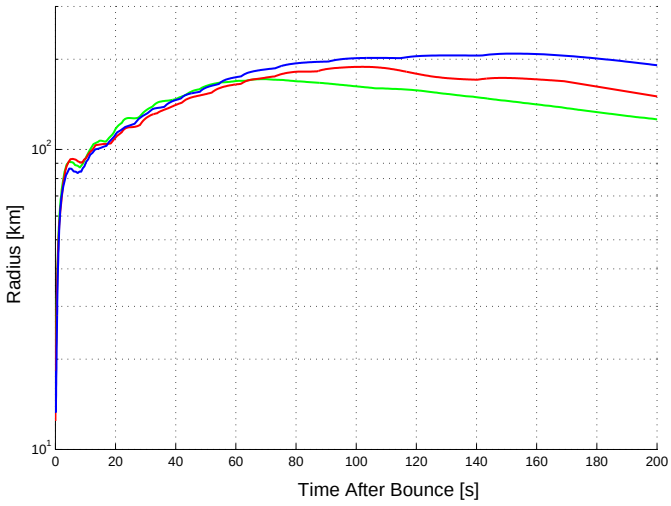

Figure 4.6: Shock trajectory with Bruenn85 rates

Chapter 5

Summary

As I have shown the Equation of State plays a large role in the collapse, bounce and post bounce evolution of a core-collapse supernova simulation. Through thermodynamic and abundance information, the EoS will drive all other physics involved under ceteris paribus situations. Using the same neutrino and hydrodynamic physics, through AGILE-BOLTZTRAN, I was able to set the various EoSs on an even playing field and see how they altered the bounce and long term evolution of the core collapse simulation. While there was general consistency in the results based on the different equations of state, there are clear differences that result directly from thermodynamic properties like stiffness, as well as secondarily as a result of differences in the composition.

In section 4.1, we demonstrated that 10 to 20% differences in the initial PNS mass can result from different EoSs. In section 4.2 we showed that changes in the EoS can affect lepton and entropy gradients in the deepest layers of the supernova well into the neutrino reheating epoch. In section 4.3, we demonstrated 20% differences in the shock location, even 200 ms after bounce, as a result of changes in the EoS.

The work in spherical symmetry presented here also lays the

groundwork for investigations of the impact of the EoS on hydrodynamical instability. Wilson's work [5, 18, 24] has provided a tantalizing preview of how instabilities may effect the long term evolution of the core collapse and post bounce evolution. Our models with Wilson's EoS also show significant differences in the lepton gradients within the PNS. Discussions on the effect that such gradients in thermodynamic quantities may have on neutron fingers and other instabilities [6, 24, 25], and their long-term effects on the core collapse simulations, must be grounded in simulations like these before they can be explored fully in multi-D to either verify or eliminate all present conjecture on their role.

Bibliography

Bibliography

[1] Lattimer, J.; Swesty, F. D. 1991, Nucl. Phys. A 535, 331.

[2] H.Shen, H.; Toki, H.; Oyamatsu, K.; Sumiyoshi, K. 1998 Nucl. Phys. A 637, 435.

[3] H.Shen, H.; Toki, H.; Oyamatsu, K.; Sumiyoshi, K. 2004 Nucl. Phys. A 730, 227.

[4] Hix, W. R.; Messer, O. E. B.; Mezzacappa, A.; Liebendörfer, M.; Sampaio, J.; Langanke, K.; Dean, D. J.; Martínez-Pinedo, G., 2003 Phys. Rev. Lett., 91, 20.

[5] Bowers, R. L.; Wilson, J. R.1982 Astrophys J. 50, 115.

[6] Bruenn, S. W.; Raley, E. A.; Mezzacappa A., astro-ph/0404099

[7] Bruenn S. W. 1985, Astrophys. J Suppl Ser., 58, 771.

[8] Mezzacappa, A.; Bruenn S. W.; 1993a, Astrophys J., 405, 637.

[9] Mezzacappa, A.; Bruenn S. W.; 1993b, Astrophys J., 405, 669.

[10] Mezzacappa, A.; Bruenn S. W.; 1993c, Astrophys J., 410, 740.

[11] Mezzacappa, A.; ARNPS, vol. 55, 467.

[12] Messer, O.E.B., Mezzacappa, A., Bruenn, S., Guidry M.W., 1998 Astrophys J., 507 353.

[13] Liebendörfer, M.; Mezzacappa, A.; Thielemann, F. K.; Messer, O. E.; Hix, W. Raphael; Bruenn, Stephen W., 2201 ,Phys. Rev. D, 63, 10.

[14] Langanke, K.; Martínez-Pinedo, G.; Sampaio, J. M.; Dean, D. J.; Hix, W. R.; Messer, O. E.; Mezzacappa, A.; Liebendörfer, M.; Janka, H.-Th.; Rampp, M. 2003, Phys. Rev. Lett., 90, .

[15] Hix, W. R.; Messer, O. E. B.; Mezzacappa, A.; Sampaio, J.; Langanke, K.; Martnez-Pinedo, G.; Liebendrfer, M.; Dean, D. J. Nuclear Physics A, 758, 31.

[16] Woosley, S. E.; Weaver, T. A. 1995 Astrophys J., Suppl. Ser.,101 181.

[17] Heger, A.; Woosley, S. E.; Martnez-Pinedo, G.; Langanke, K. 2001, Astrophys J., 560, 307.

[18] R. W. Mayle and J. R. Wilson 1991, *Calculations of neutrino heating supernovae*, S. E. Woosley, ed., New York, Springer, 333.

[19] J. R. Wilson and G. J. Mathews 2003, Cambridge Monographs on Mathematical Physics, Cambridge University Press, Cambridge.

[20] T. L. McAbee and J. R. Wilson 1994, 576, 626–638.

[21] B. Friedman, V. R. Pandharipande, and Q. N. Usmani 1981, 372, 483–495.

[22] H. Muther, M. Prakash, and T. L. Ainsworth 1987, 199, 469–474.

[23] E. Baron, J. Cooperstein, and S. Kahana 1985, 55, 126.

[24] Wilson, J. R.; Mayle, R.W.,1993, Phys. Rev., 227, 97

[25] Smarr, L.; Wilson, J. R.; Barton, R. T.; Bowers, R. L.; 1981,Astrophys. J., 246, 515.

Vita

Mark Lewis Baird was born in Norwood, Ohio, on February 28, 1972. After graduating in 1990 from Norwood High School, he enrolled in the University of Cincinnati. He temporarily left the university in December of 1990 to enlist in the United States Army, which he served in until 1998, when he received his honorable discharge. Mark graduated from the University of Cincinnati in August of 1997 with a Baccalaureate Degree in Physics. Mark received his Master of Science Degree in December of 2007.